International Journal of Fracture (2005) 136:237–264
DOI 10.1007/s10704-005-6034-9

Radial fracture during indentation by acute probes: I, description by an indentation wedging model

DYLAN J. MORRIS[1] and ROBERT F. COOK[2,3,*]
[1] *Center for Materials Research, Washington State University, Pullman, WA 99164-2711, USA*
[2] *Minneapolis, MN 55413, USA*
[3] *Present address: Ceramics Division, National Institute of Standards and Technology, Gaithersburg, MD, 20899, USA*
[*] *Author for correspondence. (E-mail: robert.cook@nist.gov)*

Received 13 July 2005; accepted in revised form 20 December 2005

Abstract. Extension of the indentation fracture toughness estimation method to very small length scales often requires the use of an indenting punch much more acute than the oft-used Vickers probe. Experimental results for very acute, sharp probes have motivated a new approach to the indentation fracture mechanics of radial crack development. An extension of the standard two-component (residual elastic–plastic + elastic contact) stress-field model of radial fracture is proposed, based on the concept that a sufficiently acute indenter can also act as a 'wedge,' prying open the surface-located radial cracks. In this, the first of a two-part series, a three-component wedging indentation model is constructed, and some general characteristics of the model are explored. In particular, the implications of the three-component stress field of the model for the description of radial crack development during load-unload indentation cycles of acute probes are considered. Explicit predictions of crack development are compared with the qualitative features of experimental observations, providing a basis for the quantitative comparisons in Part II.

Key words: Acute indenter, contact stiffness, indentation fracture, indentation wedging field, nanoindentation, radial crack, toughness.

1. Introduction

Extension of indentation toughness techniques to very small length scales (10 μm or less) is desirable for investigation of fracture properties of thin films and small volumes, but is problematic. Often it is observed that the indentation cracking threshold is substantial – that is, the indentation load beneath which the material will not crack is large. For silicate glasses, the indentation threshold for Vickers indentation is approximately 10 N (Lawn and Evans, 1977). A consequence of the threshold is that the length scales at which fracture can be studied by Vickers indentation are limited. However, cracking thresholds can be reduced dramatically, to as small as 1 mN in glasses and ceramics by employing a much more acute indenter – the cube-corner (Pharr et al., 1993). The increased damage-generating power of the cube-corner has led others to investigate fracture properties of thin films (Venkatesh et al., 2000; Li and Bhushan, 2001) and to utilize crack extension (or attenuation) as a method for residual-stress mapping on surfaces (Kese and Rowcliffe, 2003).

The above studies of crack-generation using the cube corner suggest that its crack-driving power is described by current theories of indentation fracture. However, more sophisticated indentation experiments do not wholly support the current indentation crack evolution theories, calling into question the results obtained from conventional indentation fracture interpretations. The purpose of this and the companion article (Morris et al., 2005, submitted) is to examine the tenets of the indentation fracture analysis. This is done with a view to the consequences for toughness estimation methods that use probes significantly more acute than the oft-used Vickers indenter.

2. Indentation fracture background

Strain mismatch between the plastic deformation zone generated during sharp indentation and the surrounding elastic matrix creates a reacting stress field surrounding the deformation zone that remains after contact (Lawn et al., 1980; Chiang et al., 1982). This residual elastic–plastic stress field is tensile on 'radial' planes passing through the indentation axis perpendicular to the surface and decreases with distance from the contact, giving rise to a stabilizing fracture field for cracks propagating away from the plastic deformation zone. The residual stress-intensity factor (SIF), K^{R}, for a surface-located semi-circular flaw is (Lawn et al., 1980)

$$K^{\mathrm{R}} = \chi^{\mathrm{R}} \frac{P_{\max}}{c^{3/2}}, \tag{1}$$

where $P_{\max}$ is the peak indentation load and c is the crack surface trace length (as measured from the center of the indentation impression). Originally developed for half-penny cracks (Cook and Pharr, 1990), the SIF of Equation (1) also describes radial cracks (Laugier, 1985). The amplitude of the residual SIF depends on both the material Young's modulus, E, and the hardness, H, defined as the mean supported contact stress,

$$H = \frac{P}{A} = \frac{P}{\alpha a^2}, \tag{2}$$

where A is the contact area, a is the distance from the center to an impression corner, and α relates a^2 to the projected contact area. (For example, $\alpha = \pi$ for a conical indenter, and $\alpha = 2$ for a four-sided pyramid). χ^{R} varies with the E/H ratio as (Lawn et al., 1980; Anstis et al., 1981)

$$\chi^{\mathrm{R}} = \xi^{\mathrm{R}} \left(E/H\right)^{1/2}. \tag{3}$$

ξ^{R} is a dimensionless parameter incorporating crack geometry and stress-field angular variation. ξ^{R} varies with the (axisymmetric equivalent) indenter half angle, ϕ, according to

$$\xi^{\mathrm{R}} = \zeta^{\mathrm{R}} (\cot \phi)^{2/3} \tag{4}$$

The dominance of the residual elastic-plastic field on the final crack configuration was, in part, established by monitoring radial crack evolution at Vickers indentations on a transparent specimen during the indentation load-unload cycle (Marshall and Lawn, 1979) (so-called '*in situ*' indentation fracture experiments). A two part SIF

model was presented, composed of K^{R} and a SIF attributable to the elastic contact of the indenting punch, K^{E} (Marshall and Lawn, 1979; Lawn et al., 1980):

$$K^{\mathrm{E}} = \chi^{\mathrm{E}} \frac{P}{c^{3/2}} \ln\left(\frac{2c}{a}\right), \tag{5}$$

where χ^{E} is a dimensionless SIF amplitude term. K^{E} is reversible – it is a consequence of the elastic contact stress field of the punch, and is therefore zero after the contact event. For radial cracks, χ^{E} is negative due to the compressive hoop stresses at the surface in the field of a punch (Johnson, 1999), and therefore radial crack growth is restricted during unloading until the radial cracks reach a final length in the presence of the residual field only. This was shown to be the case for Vickers indentation on soda-lime glass (Lawn et al., 1980), and also for many other transparent materials, but not all materials (Cook and Pharr, 1990). Although the initiation and evolution of radial cracks is of interest from a standpoint of fundamental understanding, the great majority of practical interest in using indentation fracture methods – to estimate material toughness, T – do not depend specifically on the manner in which radial cracks form during the indentation load–unload cycle. It is only important that the final radial crack configuration is in mechanical equilibrium with the residual field such that the condition $K^{\mathrm{R}} = T$ may be used to estimate T. In fact, published calibrations of the crack driving strength of the cube-corner suggest that the elastic–plastic model scales appropriately: ξ^{R} approximately doubles from the Vickers ($\phi = 70.3^{\circ}$) ($\xi^{\mathrm{R}} = 0.016$, experiments in silicone oil, $\xi^{\mathrm{R}} = 0.022$, experiments in air) (Anstis et al., 1981; Cook, 1985) to the cube-corner ($\phi = 42.3^{\circ}$, $\xi^{\mathrm{R}} = 0.040$, experiments in air) (Pharr, 1998), consistent with Equation (4).

Two suites of experimental results, however, suggest that reversible elastic effects may have a greater effect than previously thought, *if* the acuity of the indenting probe is great enough. The first suite of results is from *in situ* observations of cube-corner indentation on soda-lime glass and fused silica (Morris and Cook, 2004). Combination of the net SIF, Equations (1) + (5), with the toughness leads to an equilibrium fracture description of the indentation loading and unloading half-cycles as, respectively,

$$\frac{P}{c^{3/2}} = \frac{T}{\chi^{\mathrm{R}}} - \frac{\chi^{\mathrm{E}}}{\chi^{\mathrm{R}}} \frac{P}{c^{3/2}} \ln\left(\frac{2c}{P^{1/2}} (\alpha H)^{1/2}\right), \tag{6}$$

$$\frac{P_{\max}}{c^{3/2}} = \frac{T}{\chi^{\mathrm{R}}} - \frac{\chi^{\mathrm{E}}}{\chi^{\mathrm{R}}} \frac{P}{c^{3/2}} \ln\left(\frac{2c}{P_{\max}^{1/2}} (\alpha H)^{1/2}\right). \tag{7}$$

Fracture data (load and crack-length) plotted in the manner of Equations (6) and (7) will lie on a straight line of slope $-\chi^{\mathrm{E}}/\chi^{\mathrm{R}}$ and intercept T/χ^{R} if the model correctly describes the physical circumstances. Figure 1a is a plot of cube-corner indentation fracture data for both soda-lime glass and fused silica. On loading, the data for both fused silica and soda-lime glass follow a line, shown in the figure, of slope $-\chi^{\mathrm{E}}/\chi^{\mathrm{R}} = 0.50$ and intercept $T/\chi^{\mathrm{R}} = 0.48\ \mathrm{MPa\,m^{1/2}}$. During unloading, Figure 1b shows that the fracture data are clearly not represented by the same trajectory as the loading data. The same result, failure of the residual + elastic contact crack-evolution model, was also observed for both materials in a reactive environment, laboratory air.

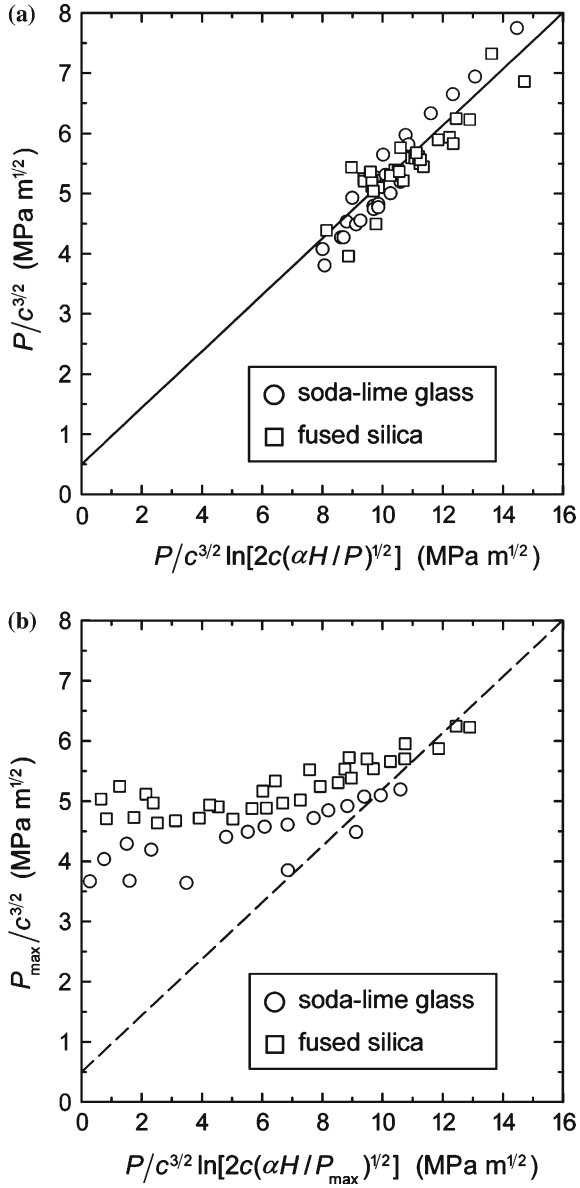

Figure 1. Indentation fracture data from *in situ* observations of cube-corner driven radial fracture on soda-lime glass and fused silica under silicone oil from (a) the loading half-cycle and (b) the unloading half-cycle. A best-fit line is drawn in (a) corresponding to slope $-\chi^{E}/\chi^{R} = 0.50$ and intercept $T/\chi^{R} = 0.48$ MPa m$^{1/2}$. This line is reproduced in (b).

In all of the cube-corner *in situ* indentation observations, crack driving forces appeared to be very large during loading – around a factor of ten too great to be consistent with the elastic-plastic residual field scaling of Equation (4) (Morris and Cook, 2004). Radial crack driving forces also appeared to be very small during subsequent unloading, resulting in relatively little or no radial crack growth. Furthermore, the apparent crack driving forces for both soda-lime glass and fused silica were indistinguishable, a curious result that has been observed elsewhere

(Pharr et al., 1993). It has long been recognized that the densification mode of deformation in fused silica (as opposed to the largely volume-conserving shear plasticity in soda-lime glass) significantly reduces the plastic strain that the matrix must accommodate (Arora et al., 1979), essentially making use of Equation (1) useless for toughness estimation with Vickers probes on fused silica (Anstis et al., 1981; Cook, 1985). It is not clear why the greater acuity of the cube-corner indenter would negate this effect.

Another set of key experimental results is from instrumented indentation, (commonly known as 'nanoindentation') experiments. Indentation load-displacement (P vs. h) behavior is a well established method for measuring elastic modulus and hardness at length scales where imaging is impractical (Oliver and Pharr, 1992, 2004). A recent study (Morris et al., 2004) investigated indentation on a variety of materials (spanning a range of E/H ratios from 9 to 200) with four three-sided pyramidal diamond probes, varying in acuity from the Berkovich to the cube-corner. The Berkovich is simply the three-sided analogue to the four-sided Vickers probe, both having an axisymmetric equivalent cone with included half angle (axis-to-face) of $\phi = 70.3^\circ$. The fracture pattern (and consequent residual SIF) generated by the Berkovich and Vickers probes were shown to be very similar (Dukino and Swain, 1992), and therefore Berkovich behavior may reliably serve as a proxy for comparison to Vickers indentation, and vice-versa. The intermediate probes are characterized by $\phi = 58.9^\circ$ and $\phi = 49.6^\circ$, and the cube-corner as $\phi = 42.3^\circ$. Two effects of radial fracture on P vs. h behavior were studied. The first was that of "pop-in," a sudden increase in displacement of the indenting probe into the surface of the material with no further increase in load when (presumably) a radial crack formed. Figure 2a is a set of three superposed P vs. h traces of indentation of fused silica by an acute diamond indenter, $\phi = 49.6^\circ$. Pop-in is seen on two of the traces, and on a third it is not. While pop-in affects the entire P vs. h response, the final plastic displacement, h_f, is unaffected. Pop-in, however, was not observed for all indentations that displayed radial fracture, and never observed for the Berkovich probe.

The second effect of radial fracture on P vs. h behavior was a distortion of the unloading (elastic recovery) response. Figure 2b plots the recovered (elastic) displacement during the unloading half-cycle for each of the four probes on fused silica. The least recovered displacement was for the most obtuse probe, the Berkovich. For more acute probes, the effect of radial fracture on the unloading behavior became greater. Indentations that did not exhibit radial fracture had unloading behavior that was completely invariant with probe geometry. In fact, while pop-in was not always observed for indentations that displayed radial fracture, distortion of the unloading behavior from the obtuse-probe response always was. Furthermore, while radial fracture was observed in micrographs at indentations by the $\phi = 58.9^\circ$ probe, there was no discernable distortion of the unloading behavior. No feature in the P vs. h behavior has been observed for radial crack initiation at Vickers indentations (Cook and Pharr, 1990).

From the instrumented indentation results, it might be surmised that there is an effect from the acuity of the indenter itself that is driving radial fracture – and that when there is fracture at the indentation site, the accompanying strain and thus displacement relief of the fracture-driving stresses are transmitted to the mechanical probe. This effect is apparently negligible for less acute probes. On unloading, the extra displacements are ultimately recovered, leading to a distortion of the unloading

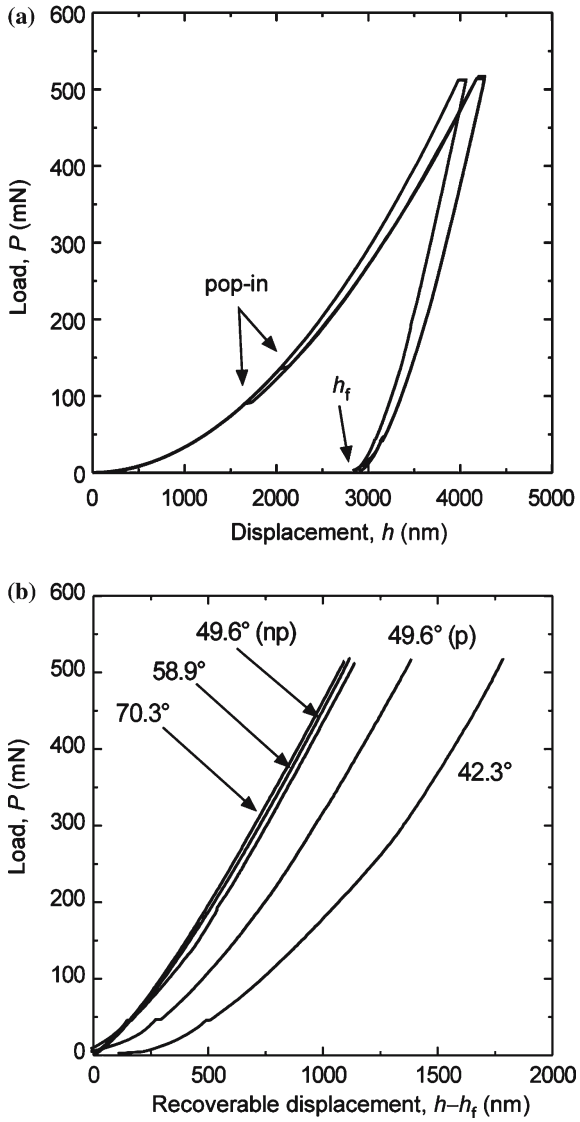

Figure 2. (a) Superposed load-displacement behavior for three 500 mN peak load contacts for an acute ($\phi = 49.6^\circ$) diamond probe on fused silica. Two indentation cycles exhibit pop-in, one does not. (b) Recovered displacement during unloading for probes of varying acuity (ϕ shown on figure) on fused silica. (np: no pop-in observed, p: pop-in observed).

curve with respect to less acute indenters. *In situ* fracture observations imply that there is a tensile, *reversible* stress field that is responsible for crack growth during loading of the indenter. Together, these experiments suggest that an acute indenter acts as an elastic 'wedge' at the material surface, driving radial fracture as the indenter is pressed into the material surface.

In the work here, a model of wedging phenomena at sharp indentation contacts is presented. The physical basis for the wedging stress field is modeled with a view towards elucidation of scaling properties with changes in indenter geometry and material properties. Indentation crack evolution in the extended three-field model

(residual + elastic contact + wedging) is compared with that in the standard two-field (residual + elastic contact) model, Equations (6) and (7). The predictions of the three-field model are compared with experimental observations of *in-situ* fracture in Part II (Morris et al., 2005, Submitted).

3. Wedging stress field

The classic result for the elastic contact stiffness, S, of an axisymmetric rigid punch in contact with an isotropic half-space is (Sneddon, 1965; Pharr et al., 1992)

$$S = \frac{2}{\pi^{1/2}} \overline{E} A^{1/2}, \tag{8}$$

where $\overline{E}$ is the plane-strain elastic modulus, $\overline{E} = E/(1-\nu^2)$, where ν is the Poisson's ratio of the material. It has been pointed out that the boundary conditions from which Equation (8) is derived prescribe displacements in the shape of a cone *normal* to the surface of the solid, but do not prescribe the *lateral* displacements, which are therefore free to take whatever form the solution generates (Akiyama et al., 1995; Hay et al., 1998). However, for any punch-material combination, unless either $\phi = 90^\circ$ (flat punch) or $\nu = 0.5$ (incompressible material), there *are* lateral displacements within the contacted zone inwards toward the indentation axis. The relative deviation within the contacted region of the material surface from the nominal shape of the punch becomes larger as the acuity of the punch increases, or as Poisson's ratio decreases. It has been shown that Poisson's ratio effects on the lateral displacement field are quite large even for (bonded) flat punches, while having little effect on the normal displacement field (Fabrikant, 1990).

For real, essentially rigid, sharp indentation, lateral displacements will be constrained such that the material conforms to the shape of the punch. The effect of the constraint of lateral displacements within the contacted zone might be expected to change the indentation stress field associated with Equation (8) commensurate with the magnitude of the deviation from the Sneddon solution. The rigid, acute indenter must push material out away from the axis of indentation as well as down, and it might be imagined that this acts much like a 'wedge,' prying open surface-intersecting cracks at the indentation. An approximate description of wedging phenomena follows.

3.1. Indentation wedging strain and stress

One effect of lateral displacement constraint will be to increase the contact stiffness over and above the prediction of Equation (8) for fixed contact area (due to the extra work needed to conform the material to the punch surface). A correction, γ, for Equation (8) was proposed (Hay et al., 1999):

$$S = \gamma \frac{2}{\pi^{1/2}} \overline{E} A^{1/2}, \tag{9}$$

where γ is greater than or equal to unity. γ is a small correction to the contact stiffness for most materials when the probe is relatively flat, such as the Berkovich probe most commonly used in instrumented indentation experiments. γ has been shown

to be a significant correction as the indenting punch becomes more acute (Hay and Pharr, 1998). The concept of 'effective' indenter geometry was introduced to relate γ to the real (axisymmetric equivalent) indenter geometry,

$$\gamma = \frac{\tan\phi_{\text{eff}}}{\tan\phi}, \tag{10}$$

where ϕ_{eff} is the half-angle of an 'effective' indenter that corrects for lateral displacement constraint. γ depends on both the half-angle of the indenter and the Poisson's ratio of the material under contact:

$$\gamma = 1 + \frac{(1-2\nu)}{4(1-\nu)\tan\phi}\left(3 - {}^{\pi}/_{2}\right). \tag{11}$$

γ is only unity when $\nu = 0.5$ or $\phi = 90^{\circ}$. ϕ_{eff} is less acute than ϕ, and in this context γ can be viewed as a correction to the projected contact area. The larger contact area of the effective indenter also means that a larger volume is displaced at a particular contact depth, with the difference in volume between the real indenter and the effective indenter approximating the volume of constrained radial displacements within the contact zone (Hay et al., 1999). Figure 3 is a schematic diagram of the material surface within the contact zone predicted by the Sneddon solution, the real rigid indenter, and the effective indenter.

If it is assumed, as a first step, that the lateral displacements are sufficiently independent of normal displacements, then an effective 'lateral volume strain' at the indentation site may be constructed by normalizing the volume of lateral displacements by the total volume displaced by the indenter. The volume, V, displaced by an axisymmetric cone from its apex to the contact depth, h_c, at a purely elastic contact is

$$V = \frac{\pi}{3} h_c^3 \tan^2\phi. \tag{12}$$

The lateral volume displaced, ΔV_{lat}, is the difference in volume between the effective cone and the assumed cone, from Equations (10) to (11). With this, the lateral volume strain is simply

$$\frac{\Delta V_{\text{lat}}}{V} = \gamma^2 - 1. \tag{13}$$

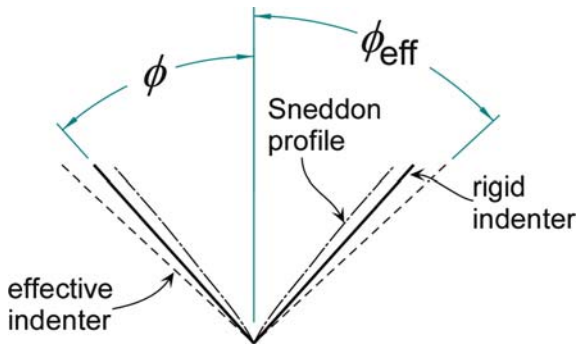

Figure 3. Schematic section-view of a sharp contact, with the real (rigid) indenter, the contact surface predicted by the Sneddon elastic solution, and the geometry of the effective indenter that compensates for the lateral displacement effect. The difference between the effective indenter and the rigid indenter approximates the volume difference between the Sneddon contact profile and the rigid indenter.

An expanding spherical cavity (or blister-field) approximation can be used to describe the stress field associated with the action of the indenting probe in the surrounding elastic matrix (Anstis et al., 1981; Chiang et al., 1982; Yoffe, 1982): Let the lateral volume strain act as a localized nucleus of strain at the surface of the material. The surface-located hemispherical blister field approximation of Yoffe (Yoffe, 1982), Appendix A, can be used to relate the lateral volume strain to wedging stresses. (See Figure 15 for the coordinate system used.) Equate the lateral displaced volume, Equation (13) to the increase in volume over a hemisphere (of any radius) caused by a blister stress field, Equation (A.4). Combination with the surface hoop stress acting at the surface over a prospective radial crack plane, Equation (A.6), yields an approximate expression for the wedging stresses acting at the surface over the prospective crack plane:

$$\sigma_\phi = \frac{1}{r^3}\left[\frac{3}{\pi}\left(\gamma^2 - 1\right)(1-\nu)\,\overline{E}\right]V. \tag{14}$$

3.2. Correction for irreversible deformation

The previous section assumed that all deformation was elastic. Sharp indentation on real materials is most frequently a combination of elastic and plastic (irreversible) deformation, so it is important to estimate the proportion of total indentation volume displaced attributable to elastic deformation only. In particular, it is important to relate the scaling of displaced elastic volume to material properties such as the elastic modulus and hardness to properly scale any indentation fracture model for material properties.

Figure 4 shows a schematic cross-sectional shape of an indentation at peak load, and the recovery it undergoes as the indenter is removed. Under load, the total displacement of the indenter apex into the surface is the sum of the contact depth, h_c, and the surface displacement, h_s,

$$h_s = \varepsilon\frac{P}{S}, \tag{15}$$

where ε is assumed to be constant and approximately equal to 0.75 (Oliver and Pharr, 1992; Pharr and Bolshakov, 2002). On unloading, the apex of the indentation impression recovers to a final depth h_f. It is assumed that there is no lateral recovery of the indentation at the surface, and that both loaded and unloaded surfaces within the contact zone are linear. This assumption will almost certainly lead to an *underestimation* of the volume accommodated by reversible deformation. Scanning probe images show significant lateral recovery within the contacted zone for fused silica (Oliver and Pharr, 2004). Perhaps more surprisingly, significant lateral recovery within the contacted zone was detected by scanning-probe techniques for a very soft material (aluminum) with virtually no apical elastic recovery (Lim and Chaudhri, 1999). (Lim and Chaudri's images also showed that there was little lateral recovery at the surface.)

If unloading from peak load is described by a power-law function of the form (Oliver and Pharr, 1992)

$$P = F(h - h_f)^m, \tag{16}$$

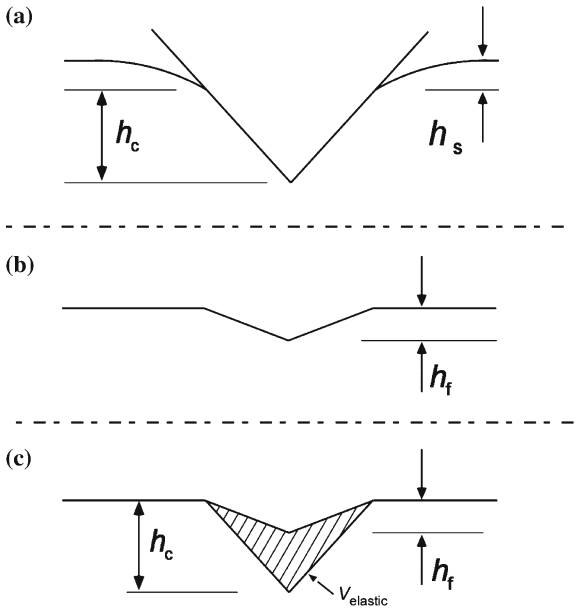

Figure 4. Volume displaced at an elastic-plastic contact. (a) Section view of a loaded material surface, with the contact displacement, h_c, and surface displacement, h_s. (b) Residual displacement, h_f, for the fully unloaded contact. At complete unload, only the displaced plastic volume is remaining. (c) Difference between the elastic–plastic (a) and plastic (b) volumes, where the frame of reference has shifted to the contact perimeter such that the elastic surface displacement is ignored. The cross-section of the elastic displaced volume, $V_{elastic}$, is shown as the hatched area.

then the elastic volume, $V_{elastic}$ (Figure 4c) may be estimated from Figure 4 with an analysis summarized in Appendix B (Wolf and Paufler, 1999):

$$V_{elastic} = \frac{\alpha \cot \phi_{edge} a^3}{3} \left[\frac{\pi^{1/2} \alpha^{1/2}}{2 \cot \phi_{edge}} \left(\frac{H}{\gamma \overline{E}} \right) (m - \varepsilon) \right], \tag{17}$$

$V_{elastic}$ is the product of the total displaced volume of the indenter, $\alpha \cot \phi_{edge} a^3 / 3$ for a pyramidal probe, and an attenuating term (in brackets) that is a function of elastic, plastic, and indenter properties. On loading, a is related to the indentation load P through the hardness relationship, Equation (2), and Equation (17) may be rewritten as

$$V_{elastic}\,(\text{loading}) = \frac{P^{3/2}}{\alpha^{1/2} H^{3/2}} \left[\frac{\pi^{1/2} \alpha^{1/2}}{6} \left(\frac{H}{\gamma \overline{E}} \right) (m - \varepsilon) \right]. \tag{18}$$

Equation (18) is valid up to peak load, P_{max}, where a is fixed at a_{max}.

Description of the manner in which the wedging field varies on unloading begins with a description of how displaced elastic volume varies on unloading. First, it is assumed that the proportion of total to elastic displaced volume remains constant during unloading, such that

$$\frac{h'_c - h'_f}{h'_c} = \left. \frac{h_c - h_f}{h_c} \right|_{P_{max}}, \tag{19}$$

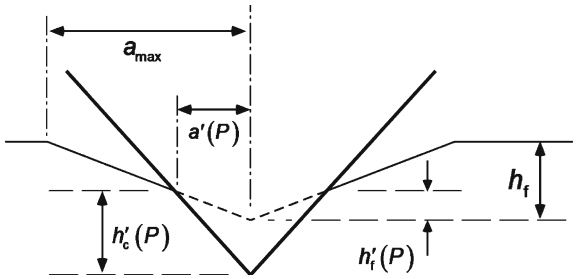

Figure 5. Volume of indentation on unloading. The fraction of indentation volume occupied by irreversible deformation is assumed to remain constant during the unloading half-cycle.

where h'_c and h'_f are defined within the frame of reference of the instantaneous contact boundary, Figure 5.

If there is only elastic recovery on unloading of the indenter, the instantaneous contact area self-adjusts to conform to the elastic stiffness relationship of Equation (9). Formation of $S = dP/dh$ by Equation (16) and combination with Equation (9) leads to the instantaneous contact dimension during unloading, $a' = h'_c \tan \phi_{edge}$:

$$a' = \frac{\pi^{1/2} m F\left(\frac{1}{m}\right) P^{\left(1-\frac{1}{m}\right)}}{2\gamma \overline{E} \alpha^{1/2}}. \tag{20}$$

At peak load, P_{max}, $a' = a_{max}$, and comparison of Equation (20) with Equation (2) shows that a' varies during the unloading cycle with P as

$$a' = \frac{P_{max}^{\left(\frac{1}{m}-\frac{1}{2}\right)} P^{\left(1-\frac{1}{m}\right)}}{(H\alpha)^{1/2}} \tag{21}$$

Substitution of Equation (21) into Equation (17) shows that the displaced elastic volume on unloading varies with load as

$$V_{elastic}\left(\text{unloading}\right) = \frac{P^{\frac{3}{m}(m-1)} P_{max}^{\frac{3}{2m}(2-m)}}{\alpha^{1/2} H^{3/2}} \left[\frac{\pi^{1/2}\alpha^{1/2}}{6}\left(\frac{H}{\gamma \overline{E}}\right)(m-\varepsilon)\right], \tag{22}$$

$V_{elastic}$ varies in the same manner on unloading as on loading ($V_{elastic} \sim P^{3/2}$, Equation (18)) only if $m = 2$. If $m = 1.5$, then $V_{elastic}$ varies linearly with load on unloading. Substitution of Equations (18) or (22) for V in Equation (14) gives the variation of the wedging stress field throughout the contact cycle.

4. Complete indentation fracture model

4.1. Stress-intensity factors during the load–unload cycle

In the indentation fracture evolution model proposed in this work, there are three operative stress fields: the residual elastic–plastic stress field, the elastic contact stress field, and the wedging stress field. Each stress-field, and corresponding SIF, varies in different ways on loading and unloading. The various SIFs are now listed separately.

As in Section 2, the residual elastic-plastic SIF, K^{R}, during the loading portion of the indentation cycle is

$$K^{\mathrm{R}}_{\mathrm{load}} = \chi^{\mathrm{R}} \frac{P}{c^{3/2}}, \tag{23}$$

where χ^{R} is a semi-empirical stress-field amplitude,

$$\chi^{\mathrm{R}} = \xi^{\mathrm{R}} \left(\frac{E}{H}\right)^{1/2} = \zeta^{\mathrm{R}} (\cot\phi)^{2/3} \left(\frac{E}{H}\right)^{1/2}. \tag{24}$$

During unloading, the plastic deformation zone is fixed and considered irreversible, and therefore the residual SIF is

$$K^{\mathrm{R}}_{\mathrm{unload}} = \chi^{\mathrm{R}} \frac{P_{\max}}{c^{3/2}}. \tag{25}$$

The second component of the fracture field is the elastic contact field. From Section 2, the elastic contact SIF during loading, $K^{\mathrm{E}}_{\mathrm{load}}$, is:

$$K^{\mathrm{E}}_{\mathrm{load}} = \chi^{\mathrm{E}} \frac{P}{c^{3/2}} \ln\left(\frac{2c}{a}\right) = \chi^{\mathrm{E}} \frac{P}{c^{3/2}} \ln\left(2c \frac{(\alpha H)^{1/2}}{P^{1/2}}\right). \tag{26}$$

This is identical to the elastic contact SIF derived by Lawn et al. (1980) for radial fracture, excepting that the logarithmic term was there considered approximately constant, and was incorporated into χ^{E}. On unloading, the inner crack boundary is fixed at $a_{\max}$, and $K^{\mathrm{E}}_{\mathrm{unload}}$ is

$$K^{\mathrm{E}}_{\mathrm{unload}} = \chi^{\mathrm{E}} \frac{P}{c^{3/2}} \ln\left(2c \frac{(\alpha H)^{1/2}}{P^{1/2}_{\max}}\right). \tag{27}$$

Equations (26) and (27) were created by substitution of the characteristic $\sigma \sim 1/r^2$ stress of the Boussinesq field, Appendix A, (while ignoring angular variations in the stress) into the weighting function for an embedded circular crack (Lawn, 1993);

$$K = \frac{2}{\pi^{1/2}} \frac{1}{c^{1/2}} \int_0^c \frac{r\sigma(r)}{\left(c^2 - r^2\right)^{1/2}} \mathrm{d}r \tag{28}$$

Completion of the integral of Equation (28) by substitution of the surface hoop stress of the Boussinesq field, Equation (A.2) (with limits $a \cdots c$ and $c^2 >> a^2$) shows that χ^{E} is related to material elastic properties through

$$\chi^{\mathrm{E}} = -\zeta^{\mathrm{E}} (1 - 2\nu), \tag{29}$$

where ζ^{E} is a positive combination constant that accounts for crack geometry, angular stress-field variations and free-surface effects.

The wedging SIF on loading, $K^{\mathrm{W}}_{\mathrm{load}}$ is created by substitution of the elastic displaced volume, Equation (18), into the surface hoop stress expression of Equation (14) and completing the integral of Equation (28) (again, with limits $a \cdots c$ and $c^2 >> a^2$):

$$K^{\mathrm{W}}_{\mathrm{load}} = \chi^{\mathrm{W}} \frac{P}{c^{3/2}}. \tag{30}$$

Here, χ^{W} performs the same function as in Equation (1): a dimensionless constant coupling material and indenter parameters to the amplitude of the stress field. χ^{W} is meant to encompass compensations for angular stress variations that were ignored in creating Equation (30), free-surface effects, and any other approximations that may have unwittingly been made. Analogous to Equation (29), ζ^{W} is the material- and geometry-independent experimental constant for the indentation wedging stress amplitude:

$$\chi^{W} = \zeta^{W} \alpha^{1/2} \frac{\left(\gamma^2 - 1\right)}{\gamma} (1 - \nu), \tag{31}$$

(A term equal to $(m - \varepsilon)$ has been incorporated into ζ^{W} for simplicity, as it is a weakly varying term with weakly established dependence on fundamental material properties, although the relationship between m and ε has been discussed at some length (Pharr and Bolshakov, 2002).) The material dependency for χ^{W} is only through Poisson's ratio – a stark contrast to the $\left(E/H\right)^{1/2}$ scaling of the elastic–plastic driving force that is normally considered a predominant characteristic of indentation fracture. On unloading, a is fixed at a_{max}, and with the unloading elastic volume expression, Equation (22), the unloading wedging SIF is created analogously to Equation (30),

$$K^{W}_{unload} = \chi^{W} \frac{P}{c^{3/2}} \left(\frac{P}{P_{max}}\right)^{\left(2 - \frac{3}{m}\right)}. \tag{32}$$

The wedging SIF retains the familiar $P/c^{3/2}$ character on unloading only if $m = 1.5$.

4.2. Total indentation fracture response

During the loading portion of the indentation cycle, the residual elastic-plastic, wedging, and elastic contact SIFs may be combined to form the total SIF, K^{T}_{load}:

$$K^{T}_{load} = \chi^{R} \frac{P}{c^{3/2}} + \chi^{W} \frac{P}{c^{3/2}} + \chi^{E} \frac{P}{c^{3/2}} \ln\left(\frac{2c}{P^{1/2}} (\alpha H)^{1/2}\right). \tag{33}$$

The scaling influence of the elastic–plastic and wedging stress-intensity factors is indistinguishable. Therefore, there is effectively a two-component fracture field during loading, with an 'effective' crack-driving amplitude, $\left(\chi^{R} + \chi^{W}\right)$. During unloading, the amplitude of the elastic–plastic mismatch field is fixed at P_{max}, and the total SIF, K^{T}_{unload}, is

$$K^{T}_{unload} = \chi^{R} \frac{P_{max}}{c^{3/2}} + \chi^{W} \frac{P}{c^{3/2}} \left(\frac{P}{P_{max}}\right)^{\left(2 - \frac{3}{m}\right)} + \chi^{E} \frac{P}{c^{3/2}} \ln\left(\frac{2c}{P_{max}^{1/2}} (\alpha H)^{1/2}\right). \tag{34}$$

The geometrical similarity of indentation fracture at sharp contacts means that Equations (33) and (34) may be normalized by an appropriate combined contact variable. Normalization is a convenient way of compactly mapping a large range of indentation fracture behavior. If hardness is assumed to be constant, as is generally true for geometrically-similar indentations if the scale of the contact is much larger than any material deformation length scale, then hardness is a characteristic stress

in the problem. Analogously, the characteristic length scale in geometrically similar indentation is a. Therefore, the unloading and loading fracture responses of Equations (33) and (34) can be normalized by a contact parameter,

$$\alpha H a_{\max}^{1/2}, \tag{35}$$

where $a_{\max} = \left(P_{\max}/\alpha H\right)^{1/2}$ (Equation (2) defines a constant, reference length scale over the entire indentation load–unload cycle). Dimensionless indentation load and crack length are defined as, respectively,

$$\begin{aligned} \overline{P} &= \frac{P}{P_{\max}}, \\ \overline{c} &= \frac{c}{a_{\max}}. \end{aligned} \tag{36}$$

Dividing Equation (33) by (35), substituting (36) and the equilibrium condition $K_{\text{load}}^{\text{T}} = T$ yields the dimensionless equilibrium fracture relationship on loading,

$$\overline{K}_{\text{load}} = \chi^{\text{R}} \frac{\overline{P}}{\overline{c}^{3/2}} + \chi^{\text{W}} \frac{\overline{P}}{\overline{c}^{3/2}} + \chi^{\text{E}} \frac{\overline{P}}{\overline{c}^{3/2}} \ln\left(\frac{2\overline{c}}{\overline{P}^{1/2}}\right) = \frac{T}{\alpha H a_{\max}^{1/2}} = \overline{T}. \tag{37}$$

The dimensionless fracture relationship on unloading is created analogously to Equation (37) with $K_{\text{unload}}^{\text{T}}$ (Equation (34)),

$$\overline{K}_{\text{unload}} = \chi^{\text{R}} \frac{1}{\overline{c}^{3/2}} + \chi^{\text{W}} \frac{\overline{P}^{\frac{3}{m}(m-1)}}{\overline{c}^{3/2}} + \chi^{\text{E}} \frac{\overline{P}}{\overline{c}^{3/2}} \ln(2\overline{c}) = \overline{T}. \tag{38}$$

5. Comparison of indentation fracture evolution models

In this section, the radial crack evolution mechanics of the three-field fracture model (residual, elastic contact, and wedging) is compared with the conventional two-field (residual and elastic contact) model. Equations (37) and (38) allow for inspection of the crack evolution models in a material-invariant way (if the SIF amplitudes, χ, may be separated temporarily from material dependence). Figure 6 is a schematic plot of $\overline{K}$ vs. $\overline{c}$. During the loading half-cycle, the fracture system moves down the $\overline{P} = 1$ line to $\overline{K}(a_{\max})$. On unloading, $\overline{K}$ is fixed, and the fracture system moves directly to the right on a line of constant $\overline{K}$, and ends at the $\overline{P} = 0$ line. By Equation (38), the $\overline{P} = 0$ line has a slope of $-3/2$ in these coordinates, and is translated up or down depending on the magnitude of χ^{R}. The $\overline{c} = 1$ line is shown. This is a minimum crack length condition stating that the radial cracks must extend out of the contact zone. The present analysis says nothing about the *initiation* of radial cracks out of the deformation zone, only that if there is sufficient driving force on a crack nucleus within the deformation zone to initiate a radial crack, then that crack can propagate to a stable length of $\overline{c}$.

For comparison purposes, fracture evolution will be modeled for soda-lime glass under contact from the two most common probes used for fracture evaluation, the Vickers indenter and the cube-corner. Table 1 shows the parameters for used for modeling – $\alpha, \chi^{\text{R}}, \chi^{\text{E}}, \chi^{\text{W}}$, and the unloading power-law exponent m, for both the two- and three-field crack evolution models. The values of $T = 0.7\,\text{MPa}\,\text{m}^{1/2}$,

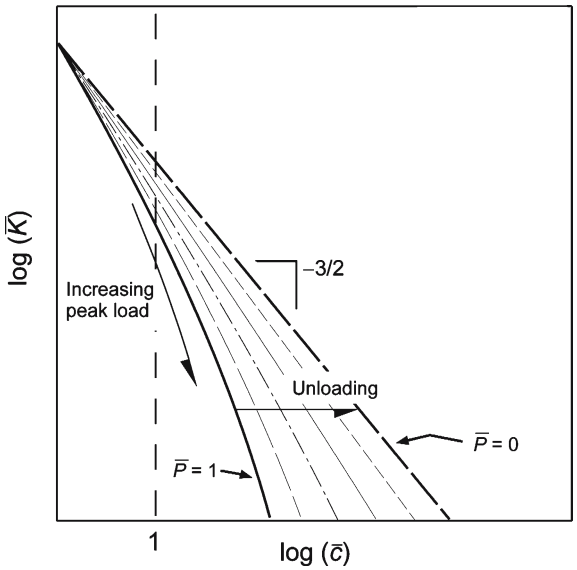

Figure 6. Example plot of $\log(\overline{K})$ vs. $\log(\overline{c})$ using the dimensionless fracture description of Equations (37) and (38). The fracture system follows the $\overline{P}=1$ trajectory during loading, and then traverses a line of constant $\overline{K}$ on unloading through lines of constant $\overline{P}$ (thin dashed lines) until $\overline{P}=0$ is reached at full unload.

Table 1. Parameters for soda-lime glass indentation fracture evolution.

Indenter/Model	α	χ^{R}	χ^{E}	χ^{W}	m
Vickers/2-field	2	0.051	−0.035	0	n/a
Vickers/3-field	2	0.051	−0.73	0.60	1.45
Cube-corner/2-field	1.3	0.082	−0.035	0	n/a
Cube-corner/3-field	1.3	0.082	−0.73	1.38	1.45

$H = 5.7$ GPa were common to all models. The origin and magnitude of these parameters are discussed in Part II of this series.

5.1. Two-field crack evolution model

Figure 7 is a plot of $\overline{K}$ vs. $\overline{c}$ for the two-field crack evolution model for soda-lime glass under Vickers indentation. Figure 7 maps quite a large range of indentation fracture behavior – a change of a factor of ten of $\overline{K}$ corresponds to a factor of 10,000 change in peak indentation load, assuming constant hardness throughout the entire span of indentation loads. A line of constant $\overline{K}$ has been drawn, corresponding to $P_{max} = 25$ N, a reasonable indentation load for toughness evaluation. Figure 8 is a pair of plots that chart the evolution of the crack length and individual stress-intensity factors for the fracture system corresponding to the $P_{max} = 25$ N line drawn in Figure 7. The two stress-intensity factors are constrained such that equilibrium is maintained through the entire indentation cycle, and always sum to a *normalized*

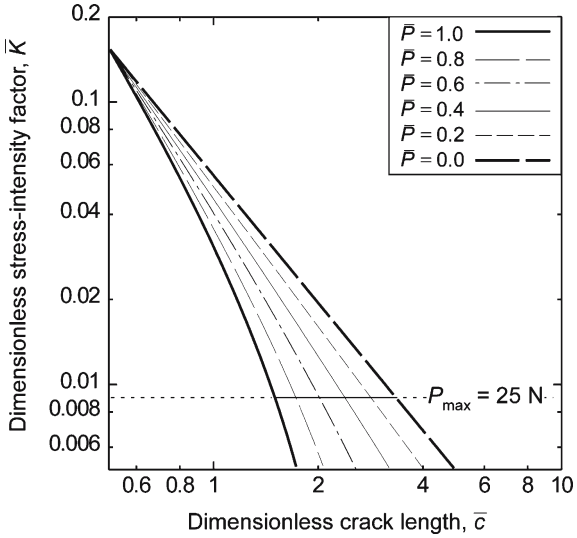

Figure 7. Dimensionless stress-intensity factor $\overline{K}$ as a function of $\overline{c}$ for Vickers indentation on soda-lime glass, calculated using the two-field model and parameters listed in Table 1. A line of constant $\overline{K}$ is shown corresponding to $P_{\max} = 25\,\mathrm{N}$.

SIF (not to be confused with the *dimensionless* SIFs of Equations. (37) and (38)) of $K/T = 1$, shown as a dashed line. At complete unload, the only SIF remaining is K^{R}.

Figure 9 is a plot of $\overline{K}$ vs. $\overline{c}$ for the two-field crack evolution model for the cube-corner indenter. The only parameter that changes from the Vickers to the cube-corner is χ^{R} and the most significant behavioral difference between the Vickers and cube-corner is the position of the $\overline{P} = 0$ line, indicative of the greater volume displaced by the cube-corner. The displacements of the line $\overline{P} = 1$ and $\overline{P} = 0$ lines show that radial cracks on loading are permissible at much smaller indentation loads than for the Vickers, consistent with experimental results that show radial cracking on loading for the cube-corner for soda-lime glass, but only on unloading for the Vickers (Morris et al., 2004). Here a $P_{\max} = 10\,\mathrm{N}$ for cube-corner indentation gives rise to a larger value than that that at $P_{\max} = 25\,\mathrm{N}$ for the Vickers. (Of course, this work is not concerned with the mechanics of crack initiation, but it stands to reason that greater driving forces for stable fracture correspond with greater driving forces for crack initiation.)

Figure 10a charts the evolution of the stress-intensity factors throughout the load-unload cycle for the $P_{\max} = 10\,\mathrm{N}$ system of Figure 9, and Figure 10b shows the simultaneous evolution of the radial cracks. There is little qualitative difference between the 25 N Vickers (Figure 8b) and 10 N cube-corner crack evolution trajectories (Figure 10b).

5.2. Three-field crack evolution model

Experimental measurements of crack-driving and resisting forces in the context of a three-field model indicate that the magnitudes of χ^{E} and χ^{W} are very large compared to χ^{R}, and the values used for demonstration of the three-field model are reflective of those results. Figure 11 is a plot of $\overline{K}$ vs. $\overline{c}$ for the three-field crack evolution model for the Vickers indenter on soda-lime glass. Comparison with the Vickers

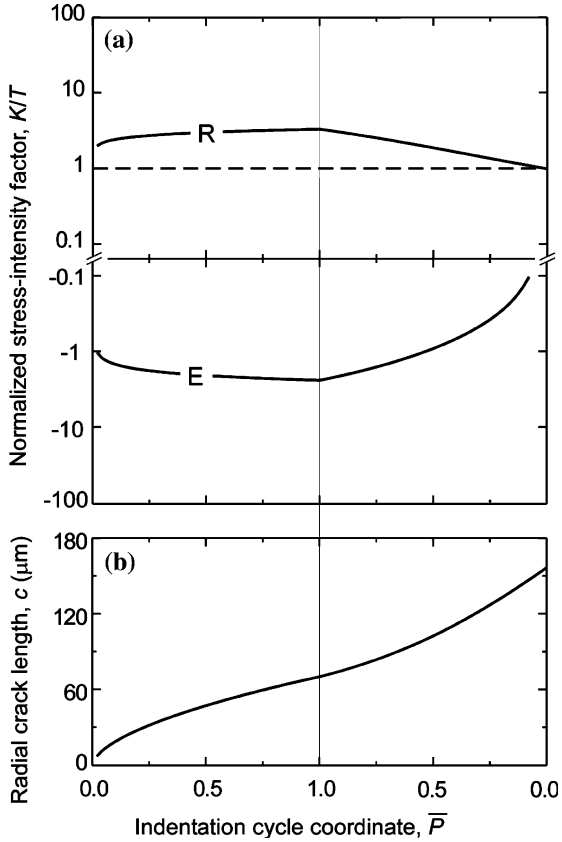

Figure 8. (a) Normalized stress-intensity factor (R – residual, E – elastic contact) evolution throughout the indentation load–unload cycle, corresponding to the $P_{max} = 25\,N$ path shown in Figure 7. At complete unload, $K^R = T$. (b) Radial crack evolution throughout the indentation load–unload cycle corresponding to the $P_{max} = 25\,N$ path shown in Figure 7.

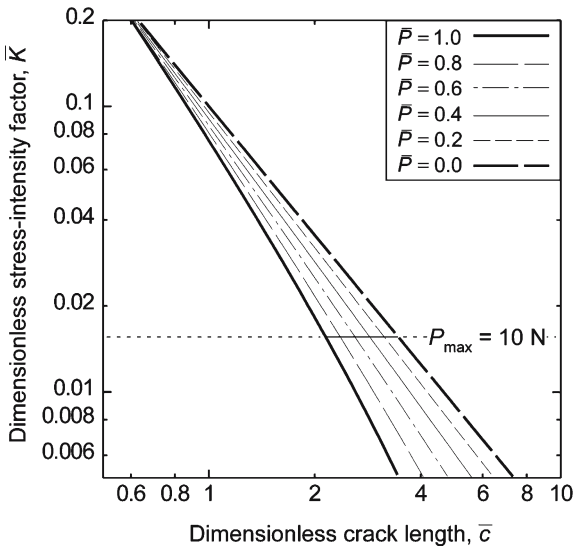

Figure 9. Dimensionless stress-intensity factor $\overline{K}$ as a function of $\overline{c}$ for cube-corner indentation on soda-lime glass, calculated using the two-field model and parameters listed in Table 1. A line of constant $\overline{K}$ is drawn corresponding to $P_{max} = 10\,N$ is shown.

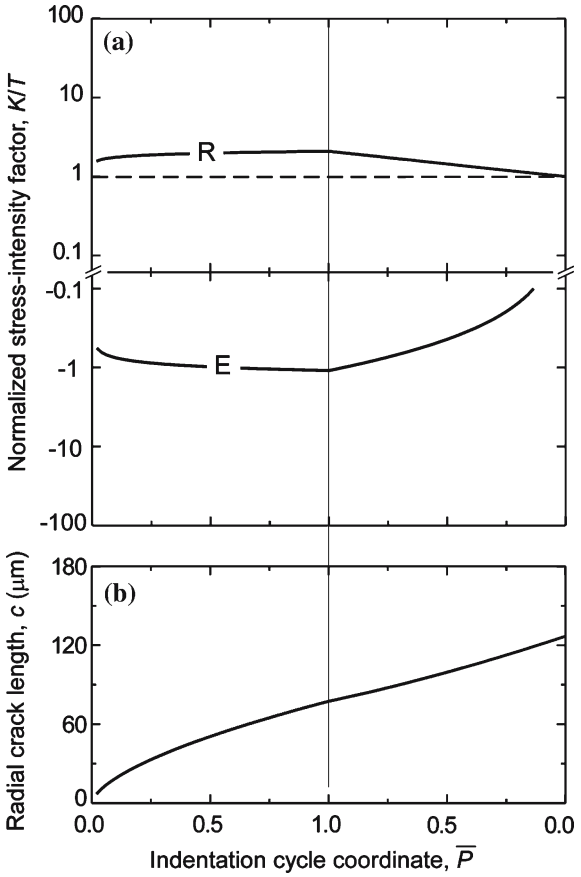

Figure 10. (a) Normalized stress-intensity factor (R – residual, E – elastic contact) evolution throughout the indentation load–unload cycle, corresponding to the $P_{max} = 10\,N$ path shown in Figure 9. At complete unload, $K^R = T$. (b) Radial crack evolution throughout the indentation load-unload cycle corresponding to the $P_{max} = 10\,N$ path shown in Figure 9.

two-field model (Figure 7) shows that the $\overline{P} = 0$ line remains invariant, as the only SIF remaining at complete unload is the residual SIF, unchanged in the comparison of the two models. However, the large, competing, wedging and elastic-contact SIFs delay the great majority of crack growth until much later in the unloading half-cycle, as illustrated in the evolution plots of Figure 12. The difference between the two- and three field models at peak load is small, and the final crack configurations are the same. While the absolute strengths of these fields are both very large compared to the residual field, the competition between the wedging and elastic-contact fields largely cancels them and allows the residual field to dominate the later stages of unloading behavior and the final crack configuration at $\overline{P} = 0$.

Figure 13a is a plot of $\overline{K}$ vs. $\overline{c}$ for the three-field crack evolution model for the cube-corner indenter on soda-lime glass. During unloading, the $\overline{K}$ vs. $\overline{c}$ relation is quite complicated, and Figure 13b is a close-up of the region in the dashed box. Figure 13b shows that on unloading from peak load, the cracks initially continue to grow. However, at some point after $\overline{P} = 0.2$, the (equilibrium) cracks would reverse direction and retract to the $\overline{P} = 0$ line.

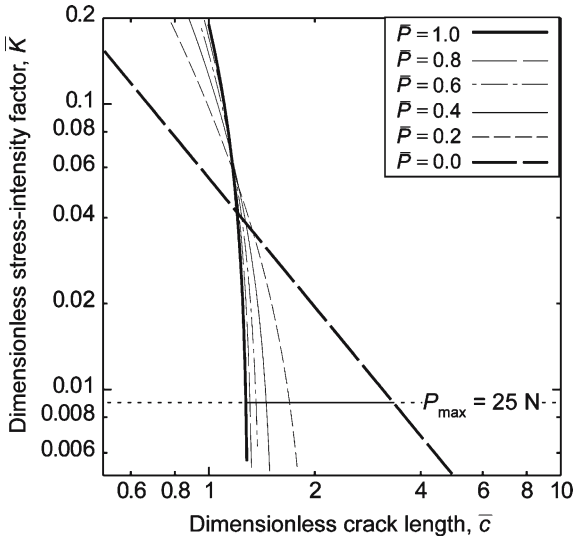

Figure 11. Dimensionless stress-intensity factor $\overline{K}$ as a function of $\overline{c}$ for Vickers indentation on soda-lime glass, calculated using the three-field model and parameters listed in Table 1. A line of constant $\overline{K}$ is drawn corresponding to $P_{max} = 25\,\mathrm{N}$ is shown.

Figure 14 plots the evolution of the individual SIFs and the radial crack length throughout the entire indentation cycle for cube-corner indentation, and demonstrates the major differences between the two-field and three-field crack evolution models. While there was little qualitative difference in the way the two-field model predicted crack evolution for the Vickers and cube-corner, the three-field model shows that a strong wedging field can disrupt normal monotonic radial crack extension during unloading. In fact, the three-field model predicts that the cracks will be much longer at peak load (slightly longer, in fact, than at complete unload for the two-field model) and that there is a maximum in crack length well within the unloading half-cycle. The cracks in the cube-corner indentation should contract in the final stages of unloading whereas those at the Vickers should extend.

6. Summary and conclusions

The two field (plastic + elastic contact) indentation fracture mechanics model, well-established for radial cracking by (rather obtuse) Vickers indenters, was found to be an inadequate description of cracking by acute indenters, typified by the cube corner. The experimental observations included: a lack of crack extension on unloading, leading to a lack of reversible fracture evolution in the appropriate (two-field) indentation fracture mechanics coordinates; a lack of dependence on the mode of plastic deformation (densification or shear) on the fracture evolution, shown to be dominant in obtuse indentation; and, the development during loading of extremely large crack driving forces that reversed on unloading, in contrast to the much smaller magnitude and irreversible crack driving forces associated with the dominant residual (plastic) field of obtuse indentation. The nature of the new, reversible, dominating, crack-driving force associated with acute indentation was elucidated by instrumented indentation measurements of load-displacement responses: an increased loading

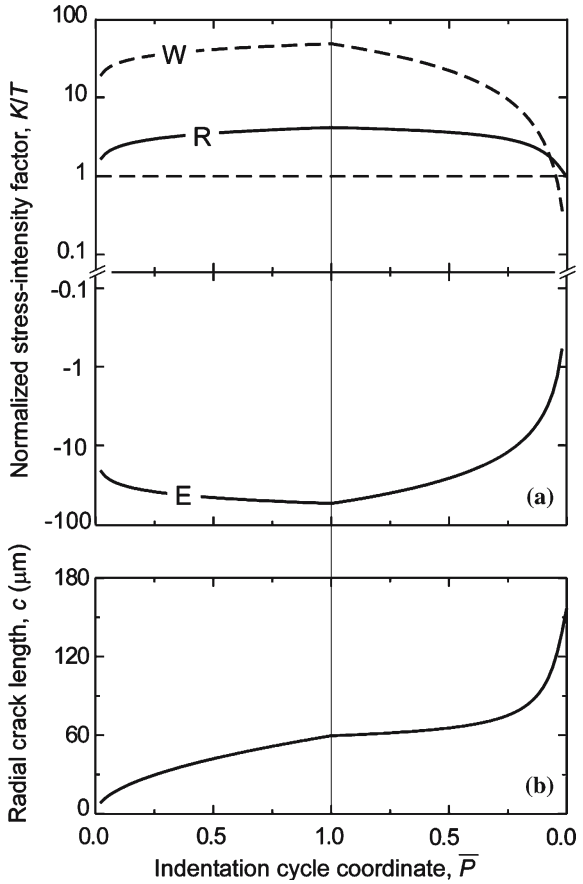

Figure 12. (a) Normalized stress-intensity factor (R – residual, E – elastic contact, W – wedging) evolution throughout the indentation load–unload cycle, corresponding to the $P_{max} = 25\,N$ path shown in Figure 11. At complete unload, $K^R = T$. (b) Radial crack evolution throughout the indentation load–unload cycle corresponding to the $P_{max} = 25\,N$ path shown in Figure 11.

compliance was observed during acute indentation, sometimes appearing as a 'pop-in' event, that was associated with the appearance of cracks; the extra deformation associated with the increased compliance was completely recovered on unloading. Taken together, the observations suggested that an indenter of sufficient acuity acts as a reversible wedge during the load–unload indentation cycle, providing a large crack driving force as the wedge presses into the material surface that is independent of, and dominates over, the residual field associated with plastic deformation, and which provides increased contact compliance as the wedge penetrates into the cracked indentation site.

The stress field associated with the wedging phenomenon was developed through perturbation of the indentation contact stiffness by elastic dilatation associated with acute probe lateral displacements, omitted in the formulation applicable to obtuse probes. Subsequent weight-function-based integration of the stress field provided the crack-driving SIF throughout the contact cycle. The analogous SIFs for the plastic and elastic contact fields were obtained by integration of the more commonly used stress fields applicable to a hemispherical blister and point contact, respectively.

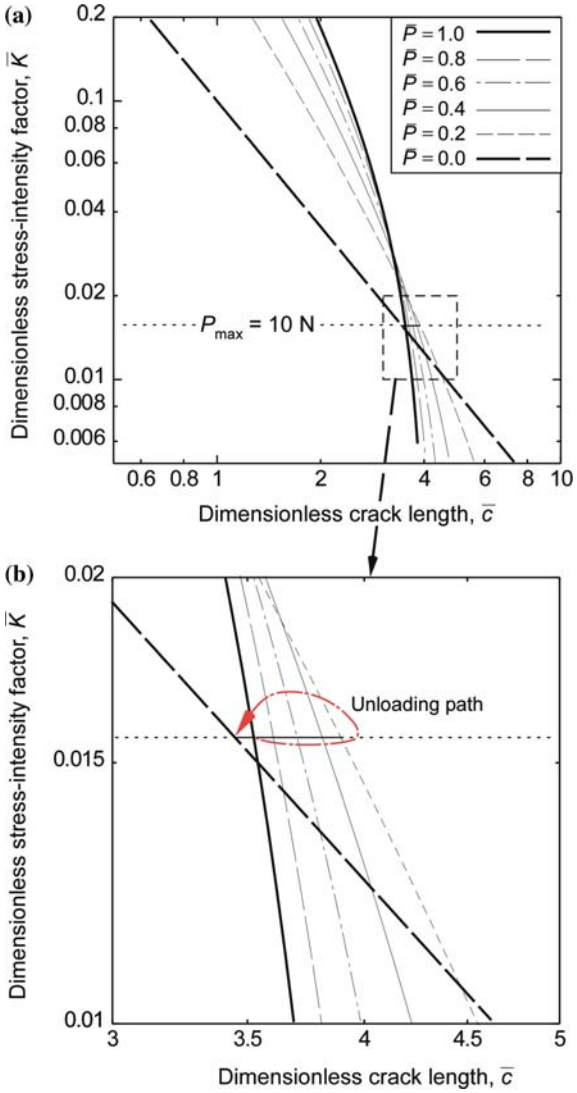

Figure 13. Dimensionless stress-intensity factor $\overline{K}$ as a function of $\overline{c}$ for cube-corner indentation on soda-lime glass, calculated using the three-field model and parameters listed in Table 1. A line of constant $\overline{K}$ is drawn corresponding to $P_{max} = 10\,N$ is shown.

The sum of these three SIFs generated a complete three-field (residual plastic + elastic contact +wedging) description of the fracture system, extending the previous two-field model to cover smaller values of the indenter included angle, 2ϕ. Imposition of the equilibrium condition provided a description of radial crack evolution throughout the contact cycle (the model could easily be modified to describe lateral crack development).

Emphasis in the analytical development was placed not so much on the functional forms of the SIFs in terms of indentation load, P, and radial crack length, c (which are quite straightforward) but on the magnitudes of the amplitude coefficients, χ^R, χ^E and χ^W (for the residual, elastic and wedging SIFs, respectively) and their scaling with ϕ and the material properties of modulus, E, Poissons's ratio, ν, and hardness,

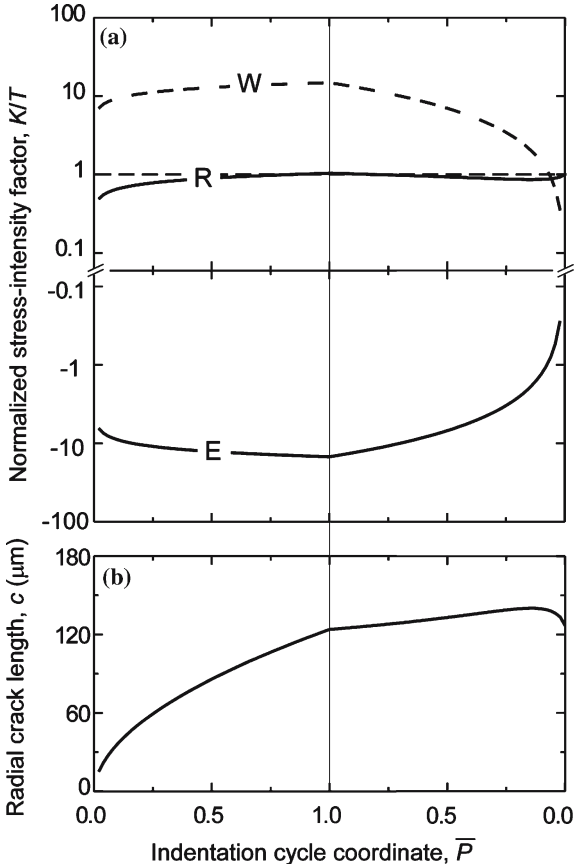

Figure 14. (a) Normalized stress-intensity factor (R – residual, E – elastic contact, W – wedging) evolution throughout the indentation load–unload cycle, corresponding to the $P_{max} = 10\,\mathrm{N}$ path shown in Figure 13. At complete unload, $K^R = T$. (b) Radial crack evolution throughout the indentation load-unload cycle corresponding to the $P_{max} = 10\,\mathrm{N}$ path shown in Figure 13.

H. The important crack driving force coefficients, χ^R and χ^W, both increase with decreasing ϕ, χ^W more strongly than χ^R, and whereas χ^R increases with the modulus/hardness ratio, E/H, χ^W does not depend on the resistances to elastic or plastic deformation at all but on the coupling between lateral and axial elastic deformation, increasing strongly with decreasing ν. Detailed quantitative comparisons of the calibrated and scaled predictions of the three-field model with experimental observations are performed in Part II, but suffice to say that for acute indenters, χ^W is about twice the magnitude of χ^E (but opposite sign, χ^E opposes radial crack development and is <0) and both are about an order of magnitude larger than χ^R. For obtuse indenters, the magnitudes of all quantities are decreased, rendering the magnitudes of χ^W and χ^E similar, but their sum comparable in magnitude, but opposite in sign, to χ^R ($\chi^W + \chi^E < 0$).

Comparison of the two- and three-field models for both Vickers and cube-corner indentation suggests that the general framework established here is able to match the qualitative details of obtuse and acute indentation observations. For obtuse indentations, the elastic and wedging SIFs combine to generate a single, reversible, radial

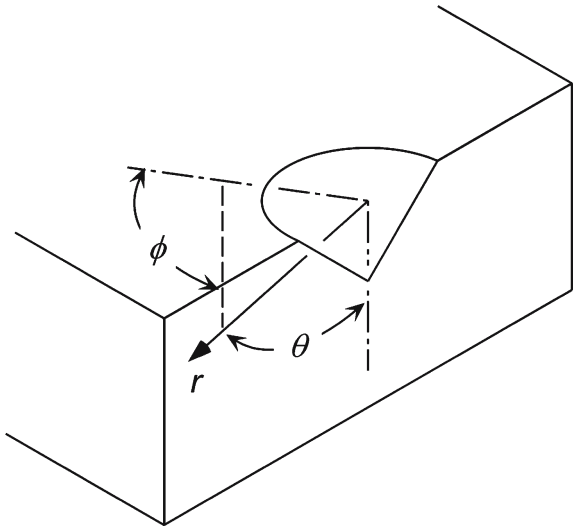

Figure 15. Schematic section through a conical indentation with angular coordinates ϕ and θ, and radial distance coordinate r, centered at the indentation.

crack opposing force (the small functional differences in their load and crack length dependence are not observable experimentally) that competes with the irreversible radial crack driving force associated with localized residual plastic deformation. A two-field description is thus appropriate. Towards the end of the contact cycle, the residual field dominates and cracks extend to remain in equilibrium with the residual field at complete unload. For acute indentations, the reversible elastic and wedging SIFs compete, essentially rendering the residual SIF irrelevant. On loading, the wedging SIF dominates, leading to large crack driving forces on loading; on unloading, both the elastic and wedging SIFs decrease to zero, leading to reduced crack driving forces. These predictions are consistent with the observations of crack extension on loading, no crack extension on unloading and no dependence on the nature of the plastic deformation. A three-field description is thus appropriate, although, to first approximation, a fully reversible two-field (elastic + wedging) model would probably describe most acute indentation fracture. The dominance of the reversible fields raises the possibility that crack lengths should actually decrease during the unloading cycle, if equilibrium were maintained. Given the extremely slow crack-healing kinetics in most brittle materials, metastable trapping of cracks in non-equilibrium configurations at their maximum length attained at the maximum driving force during the unloading cycle is probable. This suggests that toughness estimates obtained at small-scales via acute indentation fracture may well be substantially in error as the measured crack lengths reflect neither the assumed dominant residual field nor an equilibrium configuration.

Appendix A. Indentation stress fields

A short synopsis of the stress fields and observations from Yoffe (Yoffe, 1982) are reproduced below, as they are used throughout this work. Sharp indentation is modeled as a two-part stress field, made by combining the action of a punch on

the surface with a stress field that approximates a center of dilatation ('blister field') located at the surface of a half-space.

The stress field of the indentation due to the loading of the indenter may be conveniently approximated by the Boussinesq point-load solution. The Boussinesq stress field in spherical coordinates, for a point load P, is (Yoffe, 1982)

$$\begin{aligned}
\sigma_r &= \frac{P}{2\pi r^2}\,(1-2\nu-2\,(2-\nu)\cos\theta)\\
\sigma_\theta &= \frac{P}{2\pi r^2}\,\frac{(1-2\nu)\cos^2\theta}{1+\cos\theta}\\
\sigma_\phi &= \frac{P\,(1-2\nu)}{2\pi r^2}\left[\cos\theta-\frac{1}{1+\cos\theta}\right]\\
\tau_{r\theta} &= P\,\frac{(1-2\nu)}{2\pi r^2}\,\frac{\sin\theta\cos\theta}{1+\cos\theta}.
\end{aligned} \tag{A.1}$$

Relevant to radial cracking are the σ_ϕ stress components, which take a maximum compressive value at the surface ($\theta=\pi/2$),

$$\sigma_\phi\big|_{\theta=\pi/2} = -\frac{P\,(1-2\nu)}{2\pi r^2}, \tag{A.2}$$

and a maximum positive value (not considered here) directly beneath the axis of indentation.

The surface blister field is made by combining three orthogonal double forces (center of dilatation) with one opposing double force of twice the magnitude. This combination leaves a plane orthogonal to the larger double force stress- and displacement-free, and this is used as the general stress field (in the Yoffe formulation) of the elastic-plastic mismatch stresses. The displacement field of the hemispherical blister field is

$$\begin{aligned}
u_r &= \frac{B}{Gr^2}\left[2\,(1-\nu)-(5-4\nu)\cos^2\theta\right]\\
u_\theta &= \frac{B}{Gr^2}2\,(1-2\nu)\sin\theta\cos\theta,
\end{aligned} \tag{A.3}$$

where B is a measure of the strength of the field, and G is the shear modulus. As noted by Yoffe, this increases the volume of any hemisphere of radius r by the same amount,

$$\int_0^{\pi/2} 2\pi r^2 u_r \sin\theta\,\mathrm{d}\theta = \frac{4\pi B}{3\overline{E}}\,\frac{(1-2\nu)}{(1-\nu)}, \tag{A.4}$$

where $\overline{E}=2G/(1-\nu)$ has been substituted.

The stress field associated with the hemispherical blister field is

$$\begin{aligned}
\sigma_r &= \frac{B}{r^3} 4\left[(5-\nu)\cos^2\theta - (2-\nu)\right] \\
\sigma_\theta &= -\frac{B}{r^3} 2\,(1-2\nu)\cos^2\theta \\
\sigma_\phi &= \frac{B}{r^3} 2\,(1-2\nu)\left(2-3\cos^2\theta\right) \\
\tau_{r\theta} &= \frac{B}{r^3} 4\,(1+\nu)\sin\theta\cos\theta .
\end{aligned} \tag{A.5}$$

The stresses most relevant to the radial cracking system are σ_ϕ at $\theta = \pi/2$,

$$\sigma_\phi\big|_{\theta=\pi/2} = \frac{4B}{r^3}\,(1-2\nu)\,. \tag{A.6}$$

Appendix B. Estimation of displaced elastic and plastic volumes

This development follows the analysis of Wolf and Paufler (Wolf and Paufler, 1999). The elastic volume displaced at peak load is the total volume displaced by the indenter up to the contact depth, h_c, minus the residual displaced plastic volume,

$$V_{\text{elastic}} = \frac{\alpha a^2}{3}\,[h_c - h_f]\,, \tag{A.7}$$

where h_f is the final depth, that is, the displacement from the original surface where the indenter last loses contact with the material on unloading (Figure 4). If elastic unloading at an elastic-plastic contact is described by a power-law function (Oliver and Pharr, 1992),

$$P = F(h - h_f)^m, \tag{A.8}$$

then the contact stiffness, S, at $P_{\max}$ is

$$S_{\max} = \left.\frac{\mathrm{d}P}{\mathrm{d}h}\right|_{P_{\max}} = mF(h_{\max} - h_f)^{m-1}. \tag{A.9}$$

The semi-empirical relationship between h_c and the maximum displacement of the indenter into the surface of the material, $h_{\max}$, is

$$h_c = h_{\max} - \varepsilon\frac{P_{\max}}{S_{\max}} \tag{A.10}$$

where ε is a constant, roughly equal to 0.75 (Oliver and Pharr, 1992; Pharr and Bolshakov, 2002). Substitution and rearrangement of Equations (A.8) and (A.9) into (A.10) leads to

$$(h_c - h_f) = \frac{P_{\max}}{S_{\max}}\,(m - \varepsilon)\,. \tag{A.11}$$

Substitution of (A.11) into (A.7) yields

$$V_{\text{elastic}} = \frac{\alpha a^2}{3}\left[\frac{P}{S}\,(m-\varepsilon)\right]. \tag{A.12}$$

h_c, and h_f maintain geometrical similarity during the loading cycle, such that an indentation scale-invariant ratio may be formed,

$$\frac{h_c - h_f}{h_c}, \tag{A.13}$$

and the contact dimension a is linearly related to the contact depth by

$$\frac{a}{h_c} = \tan \phi_{edge} \tag{A.14}$$

where ϕ_{edge} is the included angle between the axis of indentation and the sharp edge of the indenting pyramid. Substitution of (A.13) and (A.14) into (A.12) leads to the result for the displaced elastic volume

$$V_{elastic} = \frac{\alpha a^2}{3}[h_c - h_f] = \frac{\alpha a^2 h_c}{3}\left[\frac{h_c - h_f}{h_c}\right] = \frac{\alpha a^3}{3}\left[\frac{1}{a}\frac{P}{S}(m - \varepsilon)\right]. \tag{A.15}$$

Equation (A.15) is an estimation of the displaced elastic volume that is the product of a scale-invariant term (in brackets) and an indentation volume, characterized by the cube of the characteristic contact impression length, a^3. Combination of the modified elastic stiffness relation, Equation (9), (Hay et al., 1999) with the hardness relation, Equation (2), shows that

$$\frac{P}{S} = \frac{\pi^{1/2}}{2}\alpha^{1/2} a \left(\frac{H}{\gamma \overline{E}}\right) \tag{A.16}$$

which is valid during loading, and up to peak load, if hardness and elastic modulus are invariant with load. The elastic volume displaced during loading is then a combination of Equations (A.15) and (A.16),

$$V_{elastic} = \frac{\alpha \cot \phi_{edge} a^3}{3}\left[\frac{\pi^{1/2}\alpha^{1/2}}{2 \cot \phi_{edge}}\left(\frac{H}{\gamma \overline{E}}\right)(m - \varepsilon)\right] \tag{A.17}$$

This is the product of the total volume displaced by the indenter, $\alpha \cot \phi_{edge} a^3/3$, and a plastic deformation attenuation term (in brackets).

References

Akiyama, T., Hara, T., Shibuya, T. and Koizumi, T. (1995). Axisymmetric contact problem of an elastic half-space involving tangential displacement. In: *Theoretical and Applied Mechanics*. University of Tokyo Press, Tokyo, **44**, pp. 41–49.

Anstis, G.R., Chantikul, P., Lawn, B.R. and Marshall, D.B. (1981). A critical evaluation of indentation techniques for measuring fracture toughness. I. Direct crack measurements. *Journal of the American Ceramic Society* **64**, 533–538.

Arora, A., Marshall, D.B., Lawn, B.R. and Swain, M.V. (1979). Indentation deformation/fracture of normal and anomalous glasses. *Journal of Non-Crystalline Solids* **31**, 415–428.

Chiang, S.S., Marshall, D.B. and Evans, A.G. (1982). The response of solids to elastic/plastic indentation I. Stresses and residual stresses. *Journal of Applied Physics* **53**, 298–311.

Cook, R.F. (1985). *Strength Characterisation of Ceramics Using Controlled Indentation Flaws*. Ph. D. Thesis, University of New South Wales, Sydney.

Cook, R.F. and Pharr, G.M. (1990). Direct observation and analysis of indentation cracking in glasses and ceramics. *Journal of the American Ceramic Society* **73**, 787–817.

Dukino, R.D. and Swain, M.V. (1992). Comparative measurement of indentation fracture toughness with Berkovich and Vickers indenters. *Journal of the American Ceramic Society* **75**, 3299–3304.

Fabrikant, V.I. (1990). Axisymmetric bonded punch problem: a complete solution. *Ingenieur-Archiv* **60**, 213–224.

Hay, J.C., Bolshakov, A. and Pharr, G.M. (1998). Applicability of Sneddon relationships to the real case of a rigid cone penetrating an infinite half space. In: *Materials Research Society Symposium Proceedings* Vol. 522 pp. 263–268.

Hay, J.C., Bolshakov, A. and Pharr, G.M. (1999). A critical examination of the fundamental relations used in the analysis of nanoindentation data. *Journal of Materials Research* **14**, 2296–2305.

Hay, J.C. and Pharr, G.M. (1998). Experimental investigations of the Sneddon solution and an improved solution for the analysis of nanoindentation data. In: *Materials Research Society Symposium Proceedings.* **522**, pp. 39–44.

Johnson, K.L. (1999). *Contact Mechanics*, Cambridge University Press, Cambridge.

Kese, K. and Rowcliffe, D.J. (2003). Nanoindentation method for measuring residual stress in brittle materials. *Journal of the American Ceramic Society* **86**, 811–816.

Laugier, M.T. (1985). Palmqvist crack extension and the center-loaded penny crack analogy. *Journal of the American Ceramic Society* **68**, C51–C52.

Lawn, B.R. (1993). *Fracture of Brittle Solids*, Cambridge University Press, Cambridge.

Lawn, B.R. and Evans, A.G. (1977). A model of crack initiation in elastic/plastic indentation fields. *Journal of Materials Science* **12**, 2195–2199.

Lawn, B.R., Evans, A.G. and Marshall, D.B. (1980). Elastic/plastic indentation damage in ceramics: The median/radial crack system. *Journal of the American Ceramic Society* **63**, 574–581.

Li, X.D. and Bhushan, B. (2001). Micro/nanomechanical and tribological studies of bulk and thin-film materials used in magnetic recording heads. *Thin Solid Films* **398**, 313–319.

Lim, Y.Y. and Chaudhri, M.M. (1999). Accurate determination of the mechanical properties of thin aluminum films deposited on sapphire flats using nanoindentations. *Journal of Materials Research* **14**, 2314–2327.

Marshall, D.B. and Lawn, B.R. (1979). Residual stress effects in sharp contact cracking, part I, indentation fracture mechanics. *Journal of Materials Science* **14**, 2001–12.

Morris, D.J. and Cook, R.F. (2004). *In situ* cube-corner indentation of soda-lime glass and fused silica. *Journal of the American Ceramic Society* **87**, 1494–1501.

Morris, D.J., Myers, S.B. and Cook, R.F. (2004). Sharp probes of varying acuity: instrumented indentation and fracture behavior. *Journal of Materials Research* **19**, 165–175.

Oliver, W.C. and Pharr, G.M. (1992). An improved technique for determining hardness and elastic modulus using load and displacement sensing indentation experiments. *Journal of Materials Research* **7**, 1564–1583.

Oliver, W.C. and Pharr, G.M.(2004). Measurement of hardness and elastic modulus by instrumented indentation: Advances in understanding and refinements to methodology. *Journal of Materials Research* **19**, 3–20.

Pharr, G.M. (1998). Measurement of mechanical properties by ultra-low load indentation. *Materials Science & Engineering A* **A253**, 151–159.

Pharr, G.M. and Bolshakov, A. (2002). Understanding nanoindentation unloading curves. *Journal of Materials Research* **17**, 2660–2671.

Pharr, G.M., Harding, D.S. and Oliver, W.C. (1993). Measurement of fracture toughness in thin films and small volumes using nanoindentation methods. In *NATO ASI – Mechanical Properties and Deformation Behavior of Materials Having Ultra-Fine Microstructures* (edited by) Nastasi, M. Parkin, D.M. and Gleiter, H., NATO ASI, Boston, pp. 449–461.

Pharr, G.M., Oliver, W.C. and Brotzen, F.R. (1992). On the generality of the relationship among contact stiffness, contact area, and elastic modulus during indentation. *Journal of Materials Research* **7**, 613–617.

Sneddon, I.N. (1965). The relation between load and penetration in the axisymmetric Boussinesq problem for a punch of arbitrary profile. *International Journal of Engineering Science* **3**, 47–57.

Venkatesh, T.A., Van Vliet, K.J., Giannakopoulos, A.E., and Suresh, S. (2000). Determination of elasto-plastic properties by instrumented sharp indentation: guidelines for property extraction. *Scripta Materialia* **42**, 833–839.

Wolf, B., and Paufler, P. (1999). Mechanical properties of icosahedral AlPdMn probed by indentation at variable temperatures. *Physica Status Solidi A* **172**, 341–361.
Yoffe, E.H. (1982). Elastic stress field caused by indenting brittle materials. *Philosophical Magazine A* **46**, 617–628.